Magneto-ionic control of interfacial magnetism

Uwe Bauer[1], Lide Yao[2], Aik Jun Tan[1], Parnika Agrawal[1], Satoru Emori[1], Harry L. Tuller[1],
Sebastiaan van Dijken[2] and Geoffrey S. D. Beach[1]*

In metal/oxide heterostructures, rich chemical[1,2], electronic[3–5], magnetic[6–9] and mechanical[10,11] properties can emerge from interfacial chemistry and structure. The possibility to dynamically control interface characteristics with an electric field paves the way towards voltage control of these properties in solid-state devices. Here, we show that electrical switching of the interfacial oxidation state allows for voltage control of magnetic properties to an extent never before achieved through conventional magneto-electric coupling mechanisms. We directly observe *in situ* voltage-driven O^{2-} migration in a Co/metal-oxide bilayer, which we use to toggle the interfacial magnetic anisotropy energy by $>0.75\,erg\,cm^{-2}$ at just 2 V. We exploit the thermally activated nature of ion migration to markedly increase the switching efficiency and to demonstrate reversible patterning of magnetic properties through local activation of ionic migration. These results suggest a path towards voltage-programmable materials based on solid-state switching of interface oxygen chemistry.

The physical and chemical properties of nanoscale materials derive largely from structure and composition at interfaces. The possibility to electrically modify these interfacial characteristics would provide a powerful means to control material properties. Of particular recent scientific and technological interest are metal/metal-oxide bilayers[1–15], in which properties as varied as catalytic activity[1,2], charge and spin transport[3–6], ionic exchange[14,15], mechanical behaviour[10,11], thermal conductivity[12,13] and magnetism[6–9] all depend sensitively on oxygen stoichiometry and defect structure at the metal/metal-oxide interface. Ionic transport in metal oxides can be driven by an electric field, and O^{2-} migration is already exploited as a mechanism for resistive switching in anionic metal/oxide/metal memristors[3,4]. However, the broader application of voltage-driven oxygen transport to control interfacial phenomena in metal/metal-oxide structures is only beginning to be explored.

For example, ferromagnetic metal/metal-oxide bilayers such as Co/AlO$_x$ and CoFe/MgO exhibit strong perpendicular magnetic anisotropy (PMA) derived from interfacial Co–O hybridization[8,9]. The ability to toggle interfacial PMA with a gate voltage would markedly reduce switching energies in spintronic devices, and could enable new device architectures exploiting local gating of magnetic properties[16–26]. Most work on voltage control of magnetic anisotropy in metal/metal-oxide bilayers has focused on charge accumulation or band shifting in the metal layer[16–19]. However, experimental reports of irreversibility, and anisotropy changes much larger than theoretically predicted[20,21], suggest that ionic effects may be important and in some cases even dominant[22–26]. Nonetheless, electric-field-driven oxygen migration in metal/metal-oxide bilayers is difficult to observe directly, and the impact on magnetic properties has not yet been established.

Here we report direct *in situ* observation of voltage-driven O^{2-} migration in a metal/metal-oxide bilayer, and show that solid-state electro-chemical switching of the interfacial oxidation state can be used to completely remove and restore PMA in a thin Co layer. Using cross-sectional transmission electron microscopy (TEM) and high-resolution electron energy-loss spectroscopy (EELS), we track *in situ* voltage-driven migration of the oxidation front in a Co/GdO$_x$ bilayer. By varying temperature and interface structure, we relate motion of the oxidation front to voltage-induced anisotropy changes, and show that by minimizing the O^{2-} diffusion barrier, the timescale for magneto-ionic switching can be reduced by ~6 orders of magnitude. We toggle interfacial PMA by an unprecedented $>0.75\,erg\,cm^{-2}$ at just 2 V, and achieve a magneto-electric efficiency $>5,000\,fJ\,V^{-1}\,m^{-1}$. Finally, we introduce a general method to reversibly imprint material properties through local activation of ionic migration, which we use to locally pattern magnetic anisotropy and create domain wall (DW) conduits in continuous magnetic films. These results establish magneto-ionic coupling as a powerful mechanism for voltage control of magnetism.

Experiments focus on Ta(4 nm)/Pt(3 nm)/Co(0.9 nm)/GdO$_x$ (3 nm) films sputter-deposited on thermally oxidized Si (Methods). The films exhibit strong PMA with an in-plane saturation field $H_k \sim 10\,kOe$ (Supplementary Fig. 3). Square 200 μm × 200 μm GdO$_x$(30 nm)/Ta(2 nm)/Au(12 nm) gate electrodes were patterned on top of the film for voltage application, with the bottom metal stack used as a counter electrode. Figure 1a shows a high-resolution cross-sectional TEM micrograph of the layer structure, with the thin Co layer embedded between polycrystalline Pt and GdO$_x$ layers.

Spatially resolved EELS experiments were carried out in scanning TEM (STEM) mode on the same cross-section to measure the chemical profile and to detect changes induced by a gate voltage V_g. Voltage was applied by contacting the top electrode *in situ* with a Pt/Ir tip as shown in Fig. 1a, inset (see Supplementary Information for details). Figure 1b shows representative STEM–EELS spectra with O K-edges and Co white lines from a location in the centre of the Co layer. The evolution of the O K-edge and Co L$_3$-edge count rates along a line profile perpendicular to the layers is shown in Fig. 1c. The Co layer is clearly distinguished, with no O detected within the Co layer and a sharp rise in the O signal at the Co/GdO$_x$ interface. STEM–EELS scans were then performed after applying a negative bias, which drives O^{2-} towards the Co layer. The appearance of an O K-edge signal at the centre of the Co layer can be inferred from the spectra in Fig. 1b, taken after applying −3 V for ~100 s. After subsequently applying −5 V for ~100 s, the STEM–EELS scan in Fig. 1d shows that O penetrates all the way to the bottom Co/Pt interface. Figure 1e,f demonstrates that Co oxidation is reversible under positive bias. Figure 1e shows a STEM–EELS scan after first applying a negative bias of −3 V until
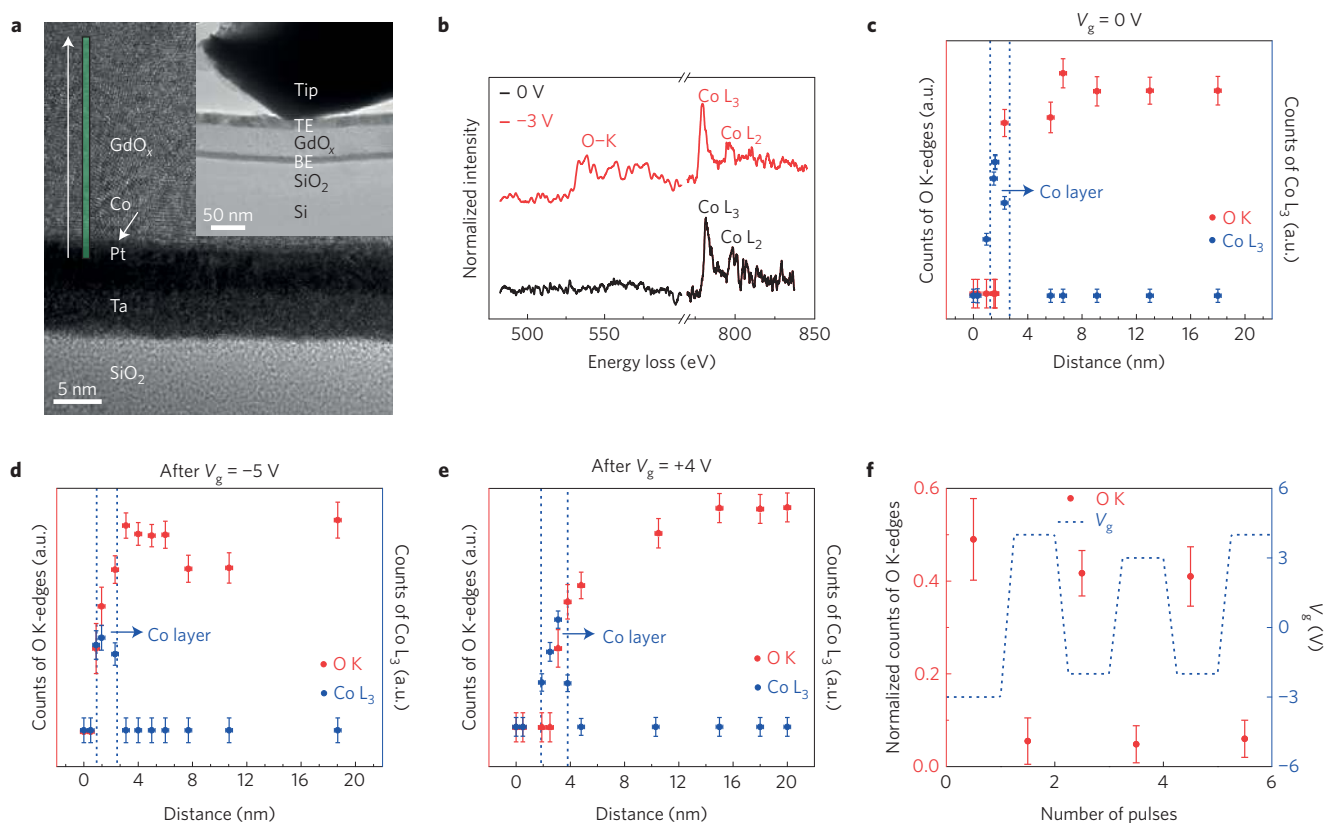

Figure 1 | Cross-sectional TEM and EELS analysis. a, High-resolution TEM image of the $SiO_2/Ta/Pt/Co/GdO_x$ layer structure. STEM–EELS spectra were measured along the green line, starting from the Pt/Co interface as indicated by the white arrow. Inset: contact between the Pt/Ir probe of the *in situ* TEM holder and the Ta/Au top electrode (TE). The Ta/Pt/Co bottom electrode is indicated by BE. **b**, STEM–EELS spectra of the O K-edges and the Co $L_{2,3}$-edges from a location in the centre of the Co layer before (black) and after (red) applying a negative bias of -3 V. **c–e**, O K-edge and Co L_3-edge count rates along a similar line profile as indicated in **a**. The data are obtained before the application of a bias voltage (**c**), after applying -5 V (**d**), and after first applying -3 V to drive O towards the Co/Pt interface, and then applying $+4$ V to drive O back away from the Co layer (**e**). **f**, O K-edge counts in the middle of the Co layer normalized to the O K-edge signal in the GdO_x layer following three cycles of alternating positive and negative bias voltage. The error bars in this figure represent the intrinsic EELS measurement noise and uncertainty during background subtraction.

an O signal was detected near the Co/Pt interface, and then applying $V_g = +4$ V for ~100 s, which drives oxygen away from the Co layer (see Supplementary Information for details). Finally, Fig. 1f shows that the O^{2-} content in the Co layer can be toggled repeatedly by cycling V_g between alternating bias polarities.

We examined the impact of voltage-induced O^{2-} migration on magnetic properties using a scanning magneto-optical Kerr effect (MOKE) polarimeter with a ~3 μm laser spot to locally probe hysteresis characteristics. Figure 2a maps the coercivity H_c in the vicinity of a gate electrode, shown schematically in Fig. 2b. Before measurement, a domain nucleation site was created nearby using a mechanical microprobe[22,23,27] so that H_c represents the DW propagation field[22,23,27], which is highly sensitive to the magnetic anisotropy energy (MAE) landscape.

In the virgin state (Fig. 2a), H_c is uniform across the measured area, reflecting a DW propagation field of ~200 Oe due to fine-scale disorder. After applying $V_g = -4$ V for 240 s and then setting $V_g = 0$ V, H_c exhibits an abrupt step at the electrode edge (Fig. 2c) and increases to ~340 Oe beneath the electrode. Similar behaviour has been observed previously[23] and attributed to O^{2-} migration near the electrode perimeter, where ionic transport is typically most efficient[28]. This would locally reduce the MAE by over-oxidizing the Co interface[8,9], creating potential wells at the electrode edge (Fig. 2d) that trap propagating DWs, increasing H_c. We verified that the DW propagation field at the interior of the electrode remained unchanged after V_g application by mechanically creating

a nucleation site inside the electrode. The observed magnetic behaviour is thus consistent with the schematic MAE landscape in Fig. 2d.

The lack of irreversible MAE changes at the electrode interior suggests that the timescale for bulk O^{2-} diffusion is much longer than at the electrode perimeter, where the open oxide edge (Fig. 2b) provides a high-diffusivity path[28]. The high ionic mobility observed in Fig. 1 is likewise probably aided by the high surface to volume ratio of the polished TEM specimen, because the activation energy for surface diffusion is typically lower than for bulk[28]. Voltage-induced O^{2-} migration, however, need not be limited to the oxide edge. Owing to the thermally activated nature of ion migration, voltage application at elevated temperature should result in exponentially higher O^{2-} drift velocities[28], and activation of bulk O^{2-} migration on an observable timescale.

Figure 2e shows a H_c map after applying $V_g = -4$ V for 155 s at $T = 100\,°C$, and then cooling the sample back to room temperature at $V_g = 0$ V. In this case, H_c outside the electrode is unchanged, showing that the elevated temperature alone does not irreversibly change the magnetic properties (Supplementary Fig. 4). However, beneath the electrode H_c drops to ~50 Oe, indicating that DWs nucleate and propagate there at a much lower field, and are impeded by an anisotropy step at the electrode edge. This implies a significant MAE reduction across the electrode area, shown schematically in Fig. 2f, consistent with overoxidation of the Co interface[8,9].
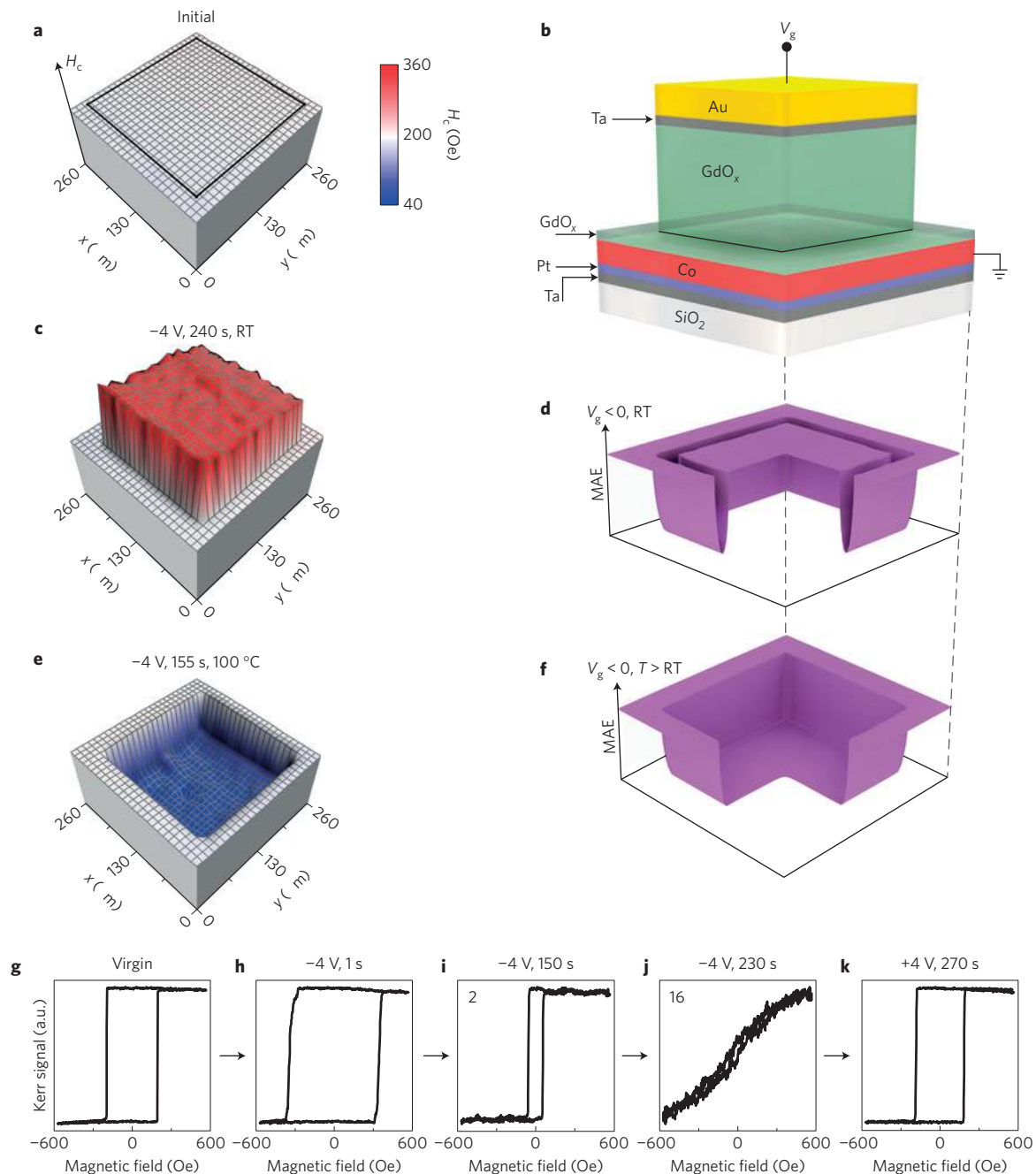
Figure 2 | Device schematics and voltage control of magnetic anisotropy. a, Topographic map of the coercivity (H_c) in the virgin state, in the vicinity of a gate electrode. **b**, Schematic view of gate-electrode structure. **c,d**, H_c and the implied MAE landscape, respectively, after applying a gate voltage $V_g = -4$ V for 240 s at room temperature (RT). **e,f**, The same as in **c,d** after applying $V_g = -4$ V for 155 s at 100 °C. **g–k**, Polar MOKE hysteresis loops measured at room temperature at the centre of the gate electrode showing the device in its virgin state (**g**), after applying $V_g = -4$ V at 100 °C for 1 s (**h**), 150 s (**i**) and 230 s (**j**), and after applying $V_g = +4$ V at 100 °C for 270 s (**k**). Note that the Kerr signal intensity in **i** is reduced by a factor of 2 and in **j** by a factor of 16, as indicated by inset number.

As seen in Fig. 2g–k, the voltage-induced MAE change at $T = 100$ °C is progressive. Here, we sequentially applied $V_g = -4$ V for a fixed dwell time at $T = 100$ °C, and then cooled the sample to room temperature with $V_g = 0$ V to measure a hysteresis loop beneath the electrode. We observe an initial increase in H_c due to DW trap formation at the electrode perimeter, which occurs within 1 s of V_g application in contrast to the several minutes required at room temperature (Fig. 2c). With increasing voltage dwell time H_c then drops precipitously, indicating a rapid reduction of PMA across the electrode. The saturation MOKE signal also declines,

by nearly a factor of 2 after ~150 s (Fig. 2i), suggesting increasing Co oxidation. After several minutes (Fig. 2j), PMA is lost entirely. Remarkably, PMA can be completely restored by reversing the bias polarity, as seen in Fig. 2k after applying $V_g = +4$ V for 270 s at 100 °C.

To correlate magnetic anisotropy with the location of the oxidation front, we used a Gd spacer to control the distance between Co and the Gd/GdO$_x$ interface. Here, GdO$_x$ was grown as a continuous 30-nm-thick layer before depositing Ta/Au electrodes to prevent DW trap formation at the edges. Figure 3a–d shows the
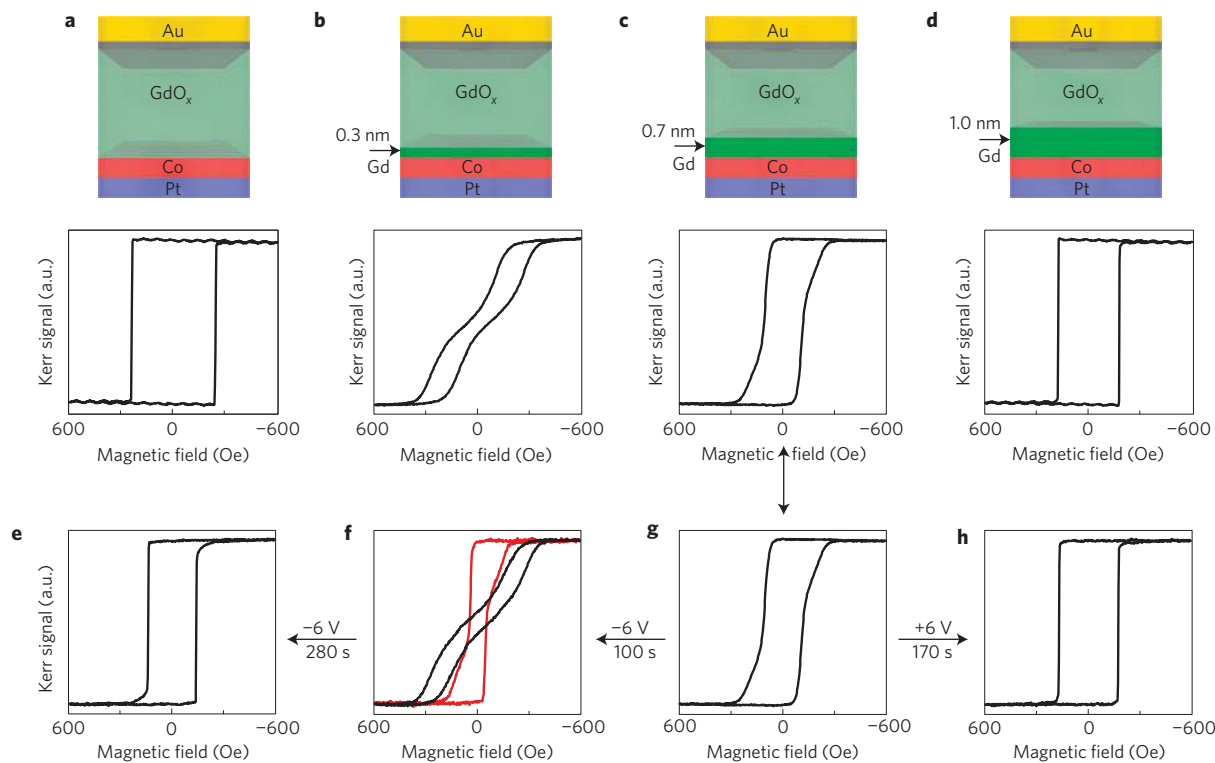
Figure 3 | Voltage-induced propagation of oxidation front. a–d, Schematics of Pt/Co/Gd/GdO$_x$ samples with different Gd spacer thicknesses (0–1 nm) at the Co/GdO$_x$ interface and polar MOKE hysteresis loops corresponding to the as-deposited samples. **e–h,** Evolution of polar MOKE hysteresis loops after application of positive (**e,f**) and negative (**h**) gate voltage V_g at 100 °C to the sample with a 0.7-nm-thick Gd spacer layer (**c,g**). All hysteresis loops were measured at room temperature and zero bias. The red curve in **f** shows a hysteresis loop after first setting the device in a state with minimum remanence ratio using a negative gate voltage, and then applying a 10 ms voltage pulse $V_g = +12$ V at 120 °C, returning the device close to its initial state.

nominal sample structure and corresponding hysteresis loops for four samples with increasing Gd spacer thickness d. With a thin Gd spacer, PMA is diminished as evidenced by a significant drop in the remanent magnetization ratio M_r/M_s (Fig. 3b), but as d is increased further, PMA again increases (Fig. 3c,d and see Supplementary Fig. 9 and related discussion for more details). We obtained similar results for other metal oxides including Pt/Co/Zr/ZrO$_x$ and Pt/Co/Ta/TaO$_x$, and find this behaviour to be rather general. The recovery of PMA for thicker metal overlayers differs from the behaviour reported in refs 8,9 for Pt/Co/Al/AlO$_x$ but is consistent with the results in ref. 29 for that system. An oscillatory dependence of PMA quite similar to our result in Supplementary Fig. 9 has also been reported for Pt/Co/Al/AlOx in ref. 30. Although the origin of this non-monotonic anisotropy variation is not well understood, it is fortuitous because it allows us to determine sensitively the position and direction of motion of the oxidation front.

Figure 3e–h shows that V_g applied to the sample in Fig. 3c completely reproduces the non-monotonic anisotropy transition exhibited by the as-deposited samples (Fig. 3a–d). With $V_g > 0$, PMA gradually increases (Fig. 3h) whereas with $V_g < 0$, PMA first decreases (Fig. 3f) then slowly increases with increasing dwell time (Fig. 3e; see also Supplementary Fig. 5). The effect of positive (negative) V_g is thus equivalent to increasing (decreasing) the spacing between Co and the oxidation front (see Supplementary Information for more details).

The results in Figs 2 and 3 demonstrate that these pronounced, non-volatile MAE changes occur through a thermally activated process, consistent with voltage-induced O^{2-} migration as observed in Fig. 1. The magnitude of the effect, which yields in Fig. 2g–k a change in interfacial PMA >0.6 erg cm^{-2}, or $\sim$5,000 fJ V^{-1} m^{-1}, corresponds to the largest magneto-electric coupling efficiency yet

reported. Although the voltage response in Fig. 2 is rather slow, because the timescale for voltage-driven ion migration exhibits a super-exponential dependence on temperature and electric field[31], faster magneto-ionic switching should be readily achieved by further increasing T and V_g. Figure 3f shows that indeed at $T = 120$ °C and $V_g = 12$ V, the timescale for anisotropy switching drops to <10 ms, compared with $\sim$100 s at 100 °C and 6 V, and in contrast to the inaccessibly long timescales required at room temperature in these devices.

To achieve similar response at room temperature and low V_g, we decreased the gate-oxide and -electrode thicknesses to reduce the O^{2-} diffusion barrier. Figure 4 summarizes results for a Ta(4 nm)/Pt(3 nm)/Co(0.9 nm)/GdO$_x$(3 nm) film on which thinner Ta(1.5 nm)/Au(5 nm) gate electrodes were sputter-deposited through a shadow mask (Fig. 4a). Figure 4d shows hysteresis loops measured at the electrode centre in the virgin state and after negative and positive voltage application, respectively, at room temperature. Here, PMA can be completely removed and restored by applying $V_g = \pm 2$ V for just $\sim$10 s, ten times faster than for the devices in Fig. 2 at higher T and V_g. These results show that a substantial reduction in the effective activation barrier for ionic motion can be achieved simply by optimizing the layer thicknesses in these devices.

To quantify the voltage-induced MAE change, we determined the anisotropy field H_k by measuring the out-of-plane magnetization M_z versus in-plane field H_x using a MOKE lock-in technique (Supplementary Information). Figure 4e shows data in the virgin state and after applying $V_g < 0$ such that PMA is reduced but the easy axis remains out-of-plane. In this case, both curves correspond to the easy-axis magnetization versus hard-axis applied field, which were fitted using the Stoner–Wohlfarth model to extract H_k. We find $H_k = 13$ kOe in the virgin state and $H_k = 700$ Oe after
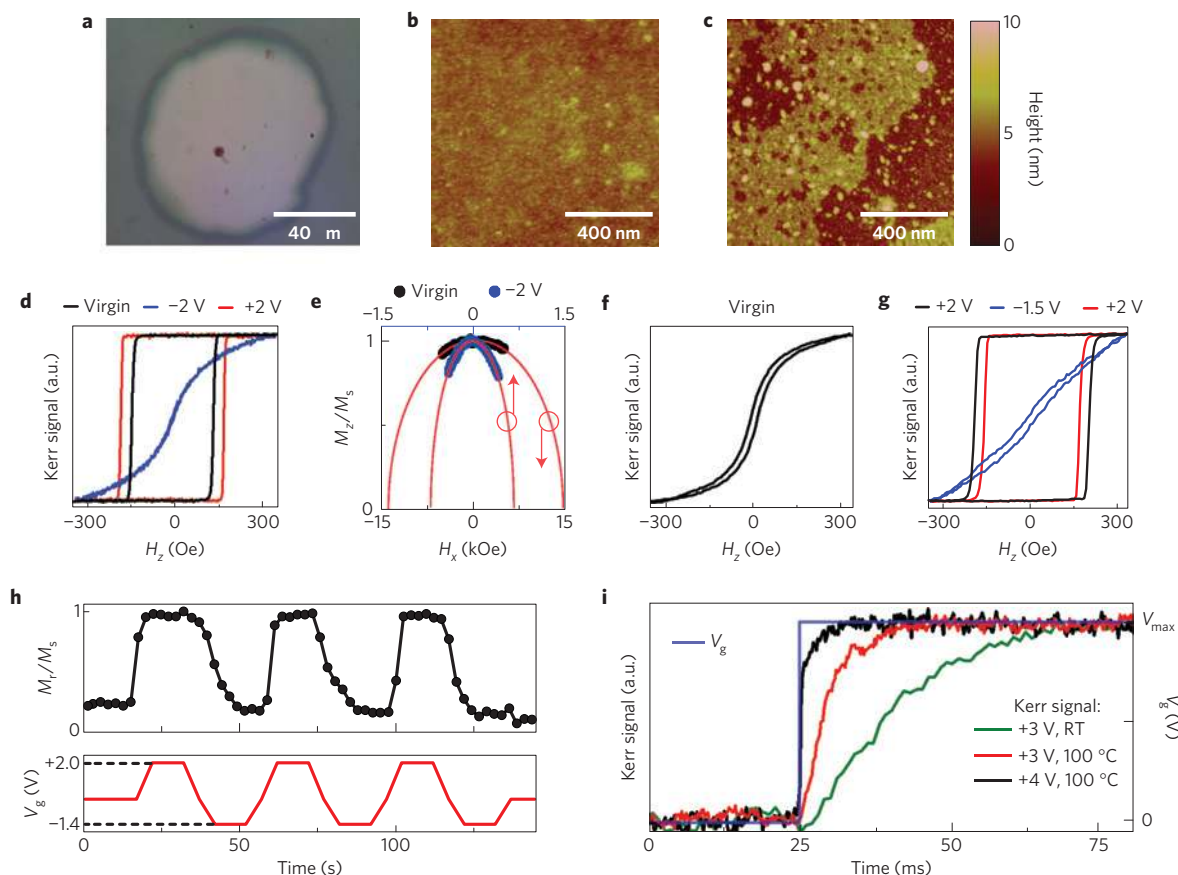
Figure 4 | Fast anisotropy switching by engineering electrode and oxide. a, Optical micrograph showing shadow-masked 100-μm-diameter Ta(1.5 nm)/Au(5 nm) gate electrode on Ta(4 nm)/Pt(3 nm)/Co(0.9 nm)/GdO$_x$(3 nm) film. **b,c**, AFM images taken at the centre (**b**) and at the edge (**c**) of a gate electrode. **d**, Polar MOKE hysteresis loops measured at the electrode centre in the virgin state and after application of a gate voltage of first $V_g = -2$ V for 10 s and then $V_g = +2$ V for 10 s at room temperature. **e**, The perpendicular magnetization component M_z measured as a function of in-plane field H_x in the virgin state (black points; with field scale on bottom axis) and after application of $V_g = -2$ V at room temperature (blue points; with field scale on top axis). The red lines are fits to the Stoner–Wohlfarth model. **f,g**, Polar MOKE hysteresis loops measured at the electrode edge in the virgin state (**f**) and after subsequent application of $V_g = +2$ V, $V_g = -1.5$ V and $V_g = +2$ V for 10 s each at room temperature (**g**). **h**, Three voltage-induced switching cycles of the remanence to saturation magnetization ratio M_r/M_s measured at the electrode edge at room temperature. **i**, Transients showing polar MOKE signal during application of a V_g pulse at room temperature (RT) and at 100 °C. A perpendicular bias field of $H_z = 40$ Oe is applied to orient the magnetization in a well-defined direction as the voltage generates PMA. V_{max} refers to the amplitude of the voltage pulse.

bias application, corresponding to a MAE reduction of at least 0.75 erg cm^{-2}.

Surprisingly, we found that even without voltage application, PMA is spontaneously diminished near the electrode perimeter (Fig. 4f) after exposure to ambient conditions for ∼24 h, suggesting that the oxygen affinity of the underlying Co layer is alone sufficient to drive O^{2-} through the GdO$_x$ there (see Supplementary Information for more details). This behaviour was restricted, however, to a ∼10 μm region at the electrode perimeter, whereas at the electrode interior and far from the electrodes, PMA is stable with time. Atomic force microscopy (AFM) shows that near its centre the electrode is continuous (Fig. 4b), but shadowing during deposition leads to a thinner region at the edge where the Au is electrically contiguous but structurally porous (Fig. 4c) owing to percolated island growth. This porous microstructure should extend the lateral extent of the triple-phase boundary, where gas phase, electrode and electrolyte coincide. Although these room-temperature effects are probably mainly aided by the reduced Au thickness and extended triple-phase boundary in these devices, the impact of reduced GdO$_x$ film thickness on O^{2-} mobility cannot, at this time, be excluded.

Figure 4g shows that the spontaneous loss in PMA in this region (Fig. 4f) can be reversed under positive V_g (Fig. 4g),

consistent with O^{2-} migration away from the Co, and that PMA can be toggled repeatedly (Fig. 4g,h). As Co redox reactions are markedly enhanced near the triple-phase boundary in these devices, it follows that faster voltage-induced switching might likewise be attained. Figure 4i shows time-resolved measurements of voltage-induced MAE switching at the electrode perimeter that directly yield the switching speed. Here, starting from the low-anisotropy state (similar to Fig. 4f), a voltage step $V_g > 0$ was applied to generate PMA while the time-resolved polar MOKE signal was measured. A small perpendicular bias field was simultaneously applied, so that as the MAE transitions from in-plane to out-of-plane, the magnetization orients in a well-defined direction. This field is too weak by itself to orient the magnetization out of the plane in the initial state, and is used only to break the symmetry so that when the easy axis switches to out-of-plane, the magnetization prefers the 'up' state over the 'down' state.

Figure 4i shows that on voltage application, the polar MOKE signal rapidly rises and saturates, indicating tilting of the magnetization out of the plane as the film transitions to PMA. The MOKE transient for $V_g = +3$ V at room temperature has a rise time of ∼25 ms, similar to the switching time achieved in Fig. 3f at $T = 120$ °C and $V_g = +12$ V, where the GdO$_x$ and Au electrodes
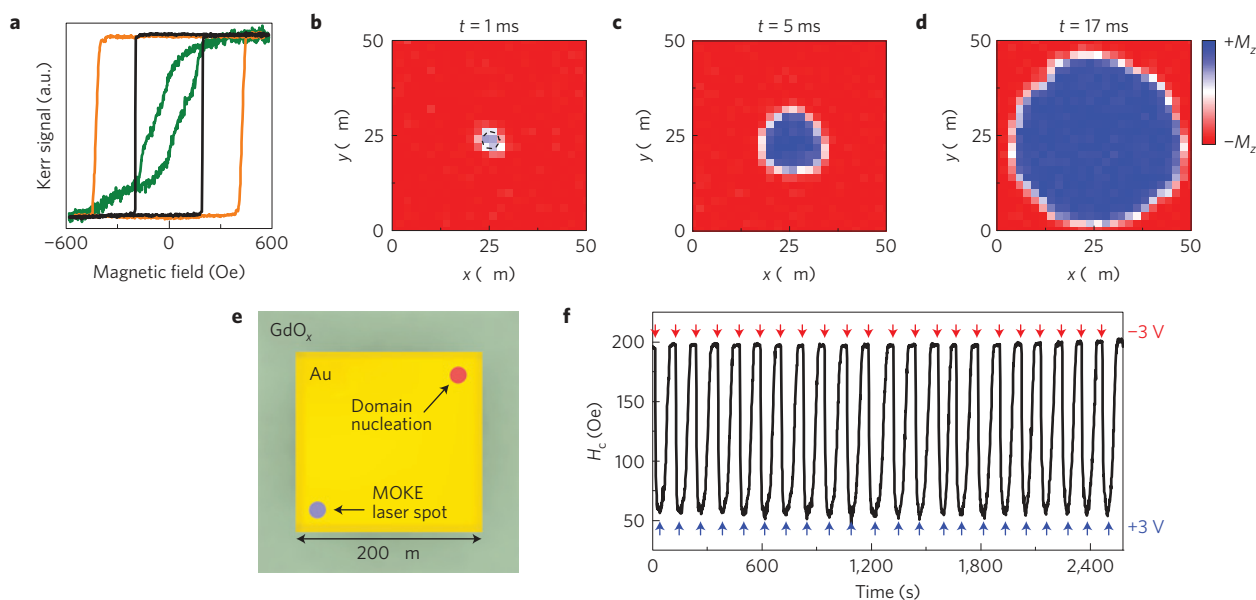
Figure 5 | Effects of voltage and laser illumination on magnetic anisotropy. a, Polar MOKE hysteresis loops measured inside a gate electrode with the device in its virgin state (black line), after application of a gate voltage $V_g = -3$ V for 90 s (orange line) and after application of $V_g = -7$ V for 180 s under laser illumination (green line). **b–d**, Snapshots of domain expansion around a laser-induced nucleation site, at the indicated times following application of a reverse field step of 90 Oe at $t = 0$. All snapshots were acquired at zero bias. The dashed black line in **b** outlines the area exposed for 100 s to the 10 mW laser spot at a gate voltage -3 V. **e**, Schematic showing top view of an electrode in which a laser-induced nucleation site has been created at the upper-right corner, and the probe laser spot is positioned at the bottom left corner. **f**, Voltage dependence of coercivity H_c as a function of V_g, corresponding to the schematic experiment geometry in **e**, as V_g is cycled between ± 3 V.

were much thicker. The switching time is further reduced by increasing T and V_g, dropping to ~700 µs at 100 °C and +4 V. The remarkable increase in switching speed, by ~6 orders of magnitude compared with the same T and V_g in Fig. 2, together with the unprecedented degree by which the MAE can be switched, indicates that magneto-ionic coupling offers a promising new route towards magneto-electric devices.

On the basis of these findings we demonstrate local MAE patterning using the MOKE laser spot to locally heat the sample and activate oxygen migration under V_g. Using the devices in Fig. 2b, we first apply $V_g < 0$ at room temperature to create a potential well at the electrode perimeter, evidenced by a jump in H_c beneath the electrode (Fig. 5a). This isolates the electrode area from DW motion in the adjacent Co film. With V_g applied, we then increase the MOKE laser power P from 1 mW to 10 mW, corresponding to a local temperature rise of ~20 °C (Methods). This causes H_c and M_r/M_s to drop markedly underneath the spot (Fig. 5a), and this change is retained when V_g is removed and P decreased to 1 mW. Neither V_g nor high P alone is sufficient to cause irreversible changes, but when both are sufficiently high (Supplementary Fig. 12), laser-induced heating activates voltage-driven O^{2-} migration, facilitating local MAE imprinting (we note that the 1 mW incident power used in the devices with thinner Ta/Au electrodes in Fig. 4 was below the threshold for laser-assisted effects for those structures).

Owing to the local anisotropy reduction, the illuminated spot acts as a domain nucleation site, as seen in the time-resolved scanning MOKE images in Fig. 5b–d (Methods). To demonstrate the reversibility of this MAE imprinting, we first created a laser-induced DW nucleation site in one corner of an electrode and then placed the laser spot in the diagonally opposite corner (Fig. 5e) with $P = 10$ mW. At $V_g = 0$ the higher laser power alone has no effect on H_c, which is determined by the field necessary to propagate a DW from the far corner. However, with $V_g = -3$ V, H_c and M_r/M_s drop markedly, indicating that instead of propagating across the electrode, DWs nucleate directly underneath the laser spot owing

to the local PMA reduction. Positive bias restores M_r/M_s and H_c to their initial values and H_c can be toggled repeatedly in this manner as V_g is cycled between +3 V and −3 V (Fig. 5f).

Finally, we imprint more complex anisotropy patterns that allow for spatial control of magnetization dynamics. In Fig. 6, we define a conduit in which DWs are injected from a laser-written nucleation site and propagate along a pre-defined path. At $V_g = -3$ V, a point inside the electrode area was illuminated at $P = 10$ mW for 100 s to produce a DW nucleation site. The laser was then scanned along an L-shaped line in 1.25 µm steps with a variable dwell time to produce a conduit of reduced MAE (Fig. 6a). Figure 6a–f shows time-resolved MOKE images of field-driven domain expansion in the patterned region (Methods). Here, a reverse domain nucleates at the laser-defined nucleation site (Fig. 6b) and expands preferentially along the laser-written conduit (Fig. 6c–f). The degree of confinement depends on the difference in MAE in the film and in the patterned region, which determines the difference in creep velocity along and orthogonal to the conduit. The DW velocity follows $v \propto \exp(-E_a(H)/k_B T)$, where the activation energy $E_a(H) \propto H^{-1/4}$ depends on the MAE (ref. 27). Figure 6g shows that the slope of $\ln(v)$ versus $H^{-1/4}$, and hence the activation energy that determines the DW velocity, can be precisely tuned to control the DW dynamics. By reducing the anisotropy in the conduit we enhance the velocity by up to a factor of ~160. The MAE can be further reduced, but in this case nucleation along the conduit is observed.

We note that local MAE patterning has previously been demonstrated using local ion beam irradiation[32,33], but has never been realized in a non-destructive and completely reversible way. Here, the spatial resolution is limited by the laser spot size to a few micrometres. However, this resolution limit could easily be overcome by instead heating the sample globally and writing the anisotropy pattern locally using, for example, a conductive AFM tip to apply V_g with high spatial resolution.

Our work shows that interfacial chemistry in metal/metal-oxide bilayers can be electrically gated using an all-solid-state
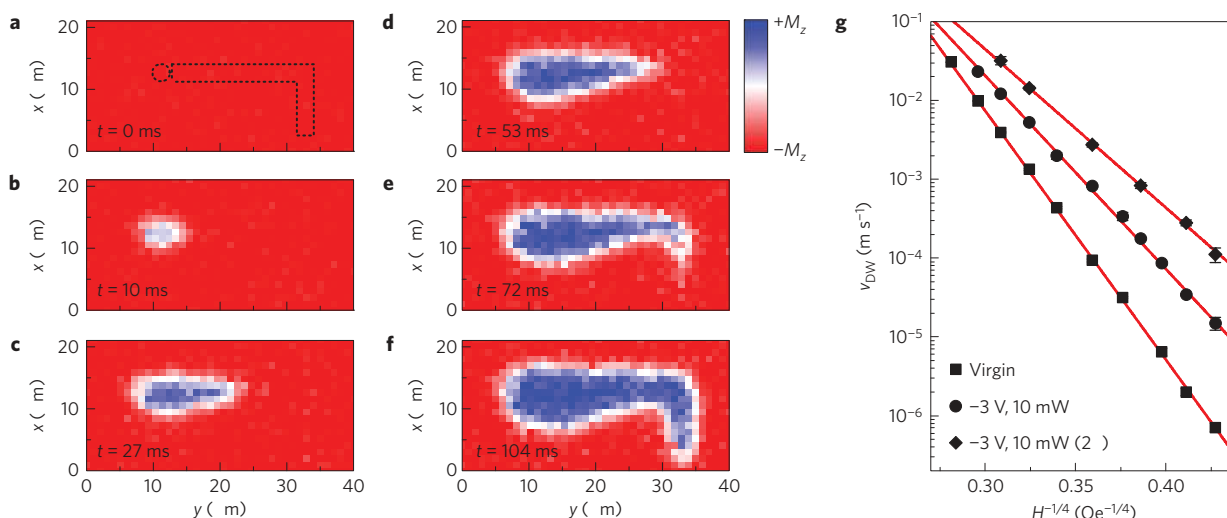
Figure 6 | Laser-defined anisotropy patterns and DW conduits. a–f, Time-resolved polar MOKE maps showing domain expansion in a laser-defined DW conduit with increasing time *t* after application of a magnetic driving field $H = 42$ Oe. Dashed black lines in **a** outline the area illuminated by the laser spot with 10 mW incident power, under gate voltage $V_g = -3$ V. The dashed circle was exposed for 100 s whereas the dashed, L-shaped line was scanned in 1.25 μm steps with 65 s exposure at each point. All maps were acquired under zero bias. **g,** DW velocity as a function of magnetic field *H* in virgin film and along a conduit exposed at 10 mW incident power under $V_g = -3$ V for 60 s and 65 s.

device, operating at low voltage and within the typical operating temperature range of common semiconductor electronics. Specifically for Co/metal-oxide bilayers, where interfacial MAE is sensitive to interface oxygen coordination, we use voltage control of oxygen stoichiometry to achieve unprecedented control over magnetic anisotropy. Moreover, we show that relatively small changes in temperature and gate voltage can improve device response times by orders of magnitude, and that by simply varying the thickness and morphology of the gate oxide and electrode, the magneto-ionic switching time drops from hundreds of seconds to hundreds of microseconds. Therefore, considerable further improvements in performance and functionality can probably be anticipated by examining oxides with higher ionic conductivity such as yttria-stabilized zirconia[15], or designing gate-oxide heterostructures that include separately optimized oxygen storage and ion conducting layers. Although this work focused on magnetic properties, reversible voltage-gated control of oxygen stoichiometry in metal/metal-oxide bilayers makes a wide range of materials properties and effects amenable to solid-state electrical control. These results thus suggest a path towards electrically gating a variety of phenomena governed by metal/oxide interfaces, and provide a new means to locally and reversibly imprint material properties by local activation of ionic migration.

Methods

Sample preparation. Ta(4 nm)/Pt(3 nm)/Co(0.9 nm)/GdO$_x$(3 nm) films were prepared by d.c. magnetron sputtering at room temperature under 3 mtorr Ar with a background pressure of ∼1 × 10^{-7} torr, on thermally oxidized Si(100) substrates. For the samples described in Fig. 3, the top GdO$_x$ layer was 30 nm thick. All GdO$_x$ layers were deposited by reactive sputtering from a metal Gd target at an oxygen partial pressure of ∼5 × 10^{-5} torr. Gate electrodes of GdO$_x$(30 nm)/Ta(2 nm)/Au(12 nm) were patterned using electron-beam lithography and lift-off. For the samples with the 30-nm-thick GdO$_x$ top layer described in Fig. 3, the Ta(2 nm)/Au(12 nm) electrodes were deposited through a shadow mask.

***In situ* high-resolution TEM characterization.** Microstructural analysis and EELS were performed on a JEOL 2200FS TEM with double Cs correctors, operated at 200 keV. A cross-sectional TEM specimen was fabricated from a patterned Si/SiO$_2$/Ta(4 nm)/Pt(3 nm)/Co(0.9 nm)/GdO$_x$(30 nm)/Ta/Au sample using the following steps. First, a Si substrate was glued to the top surface of the sample and the Si/multilayer/Si sandwich was subsequently cut into thin slices.

Next, a thin slice was polished into a wedge by a MultiPrep polishing machine (Allied High-Tech). After gluing the specimen to a half TEM Cu grid, it was further polished by Ar ion milling. Before mounting the grid onto an *in situ* electrical probing holder (HE150, Nanofactory Instruments AB), the Si was unglued from the wedge using acetone. After Si removal, a piezo-controlled Pt/Ir tip with a diameter of about 40 nm was able to contact the patterned electrode on top of the GdO$_x$ layer. Slight bending of the sample was observed after contact, but the structural integrity of the layers remained intact (Fig. 1a, inset). Silver paste was used to make electrical contact between the bottom electrode of the layer structure and the Cu grid (Supplementary Fig. 1). The thickness of the TEM specimen was estimated to be less than 30 nm by measuring the intensity ratio of the plasmon loss and the zero-loss peaks in EELS. For the analysis of EELS core-loss peaks, background subtraction was performed using a power-law fit. The lateral resolution of STEM–EELS characterization was about 0.25 nm.

MOKE measurements. Polar MOKE measurements were made using a 532 nm diode laser attenuated to 1 mW, except where noted. The laser was focused to a ∼3-μm-diameter probe spot and positioned by a high-resolution (50 nm) scanning stage with integrated temperature control. Gate voltage was applied using a mechanically compliant BeCu microprobe. Mechanically generated nucleation sites created for the measurements in Fig. 2 were prepared by applying mechanical stress to the film surface using a stiff W microprobe tip. Magnetic hysteresis loops were measured at a sweep rate of 28.3 kOe s^{-1}, using an electromagnet with a rise time of ∼300 μs and a maximum amplitude of 650 Oe.

The time-resolved domain expansion snapshots in Figs 5 and 6 were obtained by, at each pixel, first saturating the magnetization and then applying a reverse field step ($H = 90$ Oe in Fig. 5, and $H = 42$ Oe in Fig. 6) while acquiring a time-resolved MOKE signal transient. Five reversal cycles were averaged at each pixel, from which the average trajectory of the expanding domain was reconstructed.

Time-resolved MOKE transients along a line extending radially from a nucleation site were used to determine the DW velocity reported in Fig. 6g. At each position, 25 reversal cycles were acquired and averaged, yielding the cumulative probability distribution of switching times. The mean reversal time $t_{1/2}$, taken as the time at which the probability of magnetization switching is 50%, was plotted versus position, and the slope used to determine the mean velocity.

Laser-induced temperature rise. To estimate the laser-induced temperature increase ΔT, we used the temperature dependence of the coercivity of a submicrometre patterned feature. We first measured H_c versus substrate temperature, using a temperature-controlled stage and a low incident laser power (<1 mW) for the MOKE probe spot, and then measured H_c versus incident laser power P, at a fixed substrate temperature. We estimate that $P = 1$ mW corresponds to a negligible ΔT whereas $P = 10$ mW corresponds to a ΔT of at least ∼20 °C.

References

1. Stair, P. C. Metal-oxide interfaces where the action is. *Nature Chem.* **3,** 345–346 (2011).
2. Yamada, Y. *et al.* Nanocrystal bilayer for tandem catalysis. *Nature Chem.* **3,** 372–376 (2011).
3. Yang, J. J., Strukov, D. B. & Stewart, D. R. Memristive devices for computing. *Nature Nanotech.* **8,** 13–24 (2013).
4. Waser, R., Dittmann, R., Staikov, G. & Szot, K. Redox-based resistive switching memories—nanoionic mechanisms, prospects, and challenges. *Adv. Mater.* **21,** 2632–2663 (2009).
5. Jeong, J. *et al.* Suppression of metal–insulator transition in VO_2 by electric field-induced oxygen vacancy formation. *Science* **339,** 1402–1405 (2013).
6. Ikeda, S. *et al.* A perpendicular-anisotropy CoFeB–MgO magnetic tunnel junction. *Nature Mater.* **9,** 721–724 (2010).
7. Miron, I. M. *et al.* Current-driven spin torque induced by the Rashba effect in a ferromagnetic metal layer. *Nature Mater.* **9,** 230–234 (2010).
8. Manchon, A. *et al.* X-ray analysis of the magnetic influence of oxygen in $Pt/Co/AlO_x$ trilayers. *J. Appl. Phys.* **103,** 07A912 (2008).
9. Rodmacq, B., Manchon, A., Ducruet, C., Auffret, S. & Dieny, B. Influence of thermal annealing on the perpendicular magnetic anisotropy of $Pt/Co/AlO_x$ trilayers. *Phys. Rev. B* **79,** 024423 (2009).
10. Zhang, W. & Smith, J. R. Nonstoichiometric interfaces and Al_2O_3 adhesion with Al and Ag. *Phys. Rev. Lett.* **85,** 3225–3228 (2000).
11. Howe, J. M. Bonding, structure, and properties of metal-ceramic interfaces .1. Chemical bonding, chemical-reaction, and interfacial structure. *Int. Mater. Rev.* **38,** 233–256 (1993).
12. Padture, N. P., Gell, M. & Jordan, E. H. Thermal barrier coatings for gas-turbine engine applications. *Science* **296,** 280–284 (2002).
13. Losego, M. D., Grady, M. E., Sottos, N. R., Cahill, D. G. & Braun, P. V. Effects of chemical bonding on heat transport across interfaces. *Nature Mater.* **11,** 502–506 (2012).
14. Maier, J. Nanoionics: Ion transport and electrochemical storage in confined systems. *Nature Mater.* **4,** 805–815 (2005).
15. Adler, S. B. Factors governing oxygen reduction in solid oxide fuel cell cathodes. *Chem. Rev.* **104,** 4791–4843 (2004).
16. Maruyama, T. *et al.* Large voltage-induced magnetic anisotropy change in a few atomic layers of iron. *Nature Nanotech.* **4,** 158–161 (2009).
17. Wang, W. G., Li, M. G., Hageman, S. & Chien, C. L. Electric-field-assisted switching in magnetic tunnel junctions. *Nature Mater.* **11,** 64–68 (2012).
18. Shiota, Y. *et al.* Induction of coherent magnetization switching in a few atomic layers of FeCo using voltage pulses. *Nature Mater.* **11,** 39–43 (2012).
19. Duan, C. G. *et al.* Surface magnetoelectric effect in ferromagnetic metal films. *Phys. Rev. Lett.* **101,** 137201 (2008).
20. Bauer, U., Przybylski, M., Kirschner, J. & Beach, G. S. D. Magnetoelectric charge trap memory. *Nano Lett.* **12,** 1437–1442 (2012).
21. Rajanikanth, A., Hauet, T., Montaigne, F., Mangin, S. & Andrieu, S. Magnetic anisotropy modified by electric field in V/Fe/MgO(001)/Fe epitaxial magnetic tunnel junction. *Appl. Phys. Lett.* **103,** 062402 (2013).
22. Bauer, U., Emori, S. & Beach, G. S. D. Electric field control of domain wall propagation in $Pt/Co/GdO_x$ films. *Appl. Phys. Lett.* **100,** 192408 (2012).
23. Bauer, U., Emori, S. & Beach, G. S. D. Voltage-controlled domain wall traps in ferromagnetic nanowires. *Nature Nanotech.* **8,** 411–416 (2013).
24. Bonell, F. *et al.* Reversible change in the oxidation state and magnetic circular dichroism of Fe driven by an electric field at the FeCo/MgO interface. *Appl. Phys. Lett.* **102,** 152401 (2013).
25. Tournerie, N., Engelhardt, A. P., Maroun, F. & Allongue, P. Influence of the surface chemistry on the electric-field control of the magnetization of ultrathin films. *Phys. Rev. B* **86,** 104434 (2012).
26. Reichel, L., Oswald, S., Fahler, S., Schultz, L. & Leistner, K. Electrochemically driven variation of magnetic properties in ultrathin CoPt films. *J. Appl. Phys.* **113,** 143904 (2013).
27. Bauer, U., Emori, S. & Beach, G. S. D. Voltage-gated modulation of domain wall creep dynamics in an ultrathin metallic ferromagnet. *Appl. Phys. Lett.* **101,** 172403 (2012).
28. Balluffi, R. W., Allen, S. M. & Carter, W. C. *Kinetics of Materials* 209–228 (John Wiley, 2005).
29. Lacour, D. *et al.* Magnetic properties of postoxidized Pt/Co/Al layers with perpendicular anisotropy. *Appl. Phys. Lett.* **90,** 192506 (2007).
30. Dahmane, Y. *et al.* Oscillatory behavior of perpendicular magnetic anisotropy in Pt/Co/Al(O-x) films as a function of Al thickness. *Appl. Phys. Lett.* **95,** 222514 (2009).
31. Strukov, D. B. & Williams, R. S. Exponential ionic drift: Fast switching and low volatility of thin-film memristors. *Appl. Phys. A* **94,** 515–519 (2009).
32. Chappert, C. *et al.* Planar patterned magnetic media obtained by ion irradiation. *Science* **280,** 1919–1922 (1998).
33. Franken, J. H., Swagten, H. J. M. & Koopmans, B. Shift registers based on magnetic domain wall ratchets with perpendicular anisotropy. *Nature Nanotech.* **7,** 499–503 (2012).

Author contributions

U.B. and G.S.D.B. conceived and designed the experiments. H.L.T. proposed the extension of studies to higher temperatures. U.B. prepared the samples with help from A.J.T. and S.E. U.B. performed the MOKE experiments and analysed the data. P.A. and U.B. conducted the VSM and AFM measurements. S.v.D. and L.Y. performed and analysed the TEM and EELS measurements. U.B. wrote the manuscript with assistance from G.S.D.B. and input from S.v.D. and L.Y. All authors discussed the results.

Additional information

Supplementary information is available in the online version of the paper. Reprints and permissions information is available online at www.nature.com/reprints. Correspondence and requests for materials should be addressed to G.S.D.B.

Competing financial interests

The authors declare no competing financial interests.